Applied Physics Reviews ARTICLE pubs.aip.org/aip/are

Extraordinary second harmonic generation modulated by divergent strain field in pressurized monolayer domes

Cite as: Appl. Phys. Rev. **10**, 021414 (2023); doi: 10.1063/5.0144641
Submitted: 31 January 2023 · Accepted: 1 May 2023 ·
Published Online: 30 May 2023

View Online Export Citation CrossMark

Boqing Liu,[1] Tanju Yildirim,[2] Elena Blundo,[3] Domenico de Ceglia,[4] Ahmed Raza Khan,[1] Zongyou Yin,[5] Hieu T. Nguyen,[1] Giorgio Pettinari,[6] Marco Felici,[3] Antonio Polimeni,[3,a)] and Yuerui Lu[1,7,a)]

AFFILIATIONS

[1]School of Engineering, College of Engineering, Computing and Cybernetics, The Australian National University, Canberra ACT 2601, Australia
[2]Research Center for Macromolecules and Biomaterials, National Institute for Materials Science (NIMS), 1-1 Namiki, Tsukuba, Ibaraki 305-0044, Japan
[3]Dipartimento di Fisica, Sapienza Università di Roma, Roma 00185, Italy
[4]CNIT and Department of Information Engineering, University of Brescia, Brescia 25123, Italy
[5]Research School of Chemistry, College of Science, The Australian National University, Canberra ACT 2601, Australia
[6]Institute for Photonics and Nanotechnologies, National Research Council, 00133 Rome, Italy
[7]ARC Centre of Excellence in Quantum Computation and Communication Technology ANU Node, Canberra ACT 2601, Australia

[a)]**Authors to whom correspondence should be addressed:** antonio.polimeni@uniroma1.it and yuerui.lu@anu.edu.au

ABSTRACT

The most prominent form of nonlinear optical (NLO) frequency conversion is second harmonic generation (SHG), where incident light interacts with a nonlinear medium producing photons at double the input frequency, which has vast applications in material and biomedical science. Emerging two-dimensional nonlinear optical materials led by transition metal dichalcogenides (TMDs) have fascinating optical and mechanical properties and are highly anticipated to overcome the technical limitations imposed by traditional bulky NLO materials. However, the atomic scale interaction length and low conversion efficiency in TMD materials prevent their further implementation in NLO applications. While some uniaxial strain-engineering studies intensively investigated the anisotropic SHG response in TMDs, they did not realize giant SHG enhancement by exploiting the opto-mechanical characteristics. Herein, we employ proton (H^+) irradiation to successfully fabricate large pressurized monolayer TMD domes ($d \geq 10\,\mu$m) and conduct a comprehensive investigation and characterization of their SHG performance enhancement. We show that the intensity of SHG is effectively enhanced by around two orders of magnitude at room temperature. Such giant enhancement arises from the distinct separation distance induced by capped pressurized gas and the hemi-spherical morphology, enabling constructive optical interference. Moreover, the unique divergent strain field in TMD domes promotes the first experimental study on the anisotropic nonlinear optical behavior based on biaxial strain conditions in terms of varying strain orientation and relative weights. Our work demonstrates a promising system with enhanced NLO performance and well-preserved biocompatibility, paving a way toward the future nano-scaled quantum optics design and biomedical applications.

INTRODUCTION

Materials with broken inversion symmetry possess a non-vanishing second-order nonlinear optical susceptibility, $\chi_0^{(2)}$. When these materials are exposed to an intense optical pump, they can give rise to strong second-harmonic generation (SHG), resulting in the frequency doubling of a light wave. Such a strong nonlinear frequency conversion process has paramount importance for applications, including light generation, quantum photonics, optical signal processing, and imaging.[1–5] Furthermore, SHG is frequently utilized to identify material properties, such as crystal symmetry, band structure,[6,7]

lattice orientation,[8,9] polar domains and magnetic ordering,[10] surfaces, and quantum interference.[11] On the other hand, due to the weak photon–photon interactions in traditional nonlinear optical (NLO) materials, the high SHG output heavily relies on large pumping power, bulky interaction volumes, and proper phase-matching conditions. This becomes the substantial challenge in miniaturized nonlinear optical devices for future applications. The emergence of two-dimensional nonlinear materials is anticipated to provide the solution for novel nonlinear optics to overcome the technical limit imposed by traditional NLO materials. One of the most outstanding candidates is transition metal dichalcogenides (TMD) of the form MX_2 (M = Mo, W and X = S, Se). As one transition metal atom is sandwiched between two layers of chalcogen atoms in each monolayer TMD crystal, broken inversion symmetry only exists in TMD crystals having an odd number of layers, which leads to a large second-order susceptibility $\chi_0^{(2)}$ and strong SHG intensities at the atomic thickness level.[12–15] In addition, TMD films also possess remarkable mechanical flexibility and robustness, enabling them to withstand large stretching and mechanical deformation,[16–19] and have great potential for flexible optical devices.

Currently, one of the primary barriers in the practical application of TMD materials' SHG capability is the atomically thin light–matter interaction length scale, resulting in low conversion efficiency. The common approaches for enhancing SHG intensity heavily rely upon external hardware setups including photonic crystal resonators[20–22] and external voltage modulation,[22,23] which have limited applicability due to tedious sample preparation and fabrication processes. In contrast, strain-engineering techniques can effectively manipulate optical properties and bring novel features,[24] including strain induced bandgap modulation,[25,26] exciton funneling effects,[16] and single photon emission.[27,28] While some work claimed heavy SHG emission quenching caused by applied strain,[29,30] a previous report using a wrinkling technique achieved moderate enhancement in SHG emssion,[31] meaning strain has adverse effects on SHG emission. At the same time, previous strain engineering approaches primarily focused on the anisotropic SH response under uniaxial strain,[24,30–33] instead of SHG enhancement. This condition appears to imply that traditional strain engineering fails to capitalize on the mechanical features of TMD materials and their resulting SHG performance.

In this work, we successfully fabricate pressurized monolayer TMD domes with radii up to a few micro-meters and conduct comprehensive SHG measurements. The hemi-spherical geometry of domes and large internal gas pressure effectively improve SHG emission with two orders of magnitude at room temperature and one order of magnitude enhancement at −190 °C, compared to the unstrained TMD monolayer flakes in the C exciton peak range. Moreover, taking advantage of enhanced SHG responses and unique diverging strain field in TMD domes, we first experimentally investigate and reveal the influence of biaxial strain on the anisotropic SHG response. The minor evolution of the lattice distortion caused by biaxial strain in various magnitudes and directions is clearly probed via polarization resolved SHG, and corresponding anisotropic responses are clearly depicted in SHG polar plots. According to our work, we believe TMD domes exhibiting extraordinary SHG emission will become promising candidates for future nonlinear optical devices and biomedical imaging and sensing devices.

RESULTS AND DISCUSSION

SHG mechanism in dome structures

In this work, the dome formation was achieved by the proton (H^+) irradiation method. By being accelerated by an electric field, protons penetrate the top few layers of TMD flakes and subsequently reduce to hydrogen gas, trapped beneath the flake's uppermost few layers.[34] The competition between interlayer adhesion energy, elastic energy of the TMD film, and pressure of the capped gas reaches an equilibrium state, forming stable domes [Fig. 1(a)][35,36] that have a universal shape and endure for a very long time without any structural changes.[37,38] This method allows domes to range in sizes from a few to dozens of micrometers, making it possible to conduct SHG measurements on domes as well as other far field optical studies.[39,40] As TMD domes would serve as the local suspension, those with an odd number of layers would become the nonlinear optical emitters grown on the bulk flake [Fig. 1(b)]. By conducting SHG mapping measurements on the dome samples, we found that most domes are monolayer as they have strong SHG emission compared to the bulk flake.

For different dome sizes, the strongest emission zones are not consistently found at the center. This fact could be explained as optical interference occurred within the dome structure. When the fundamental light (near infrared light source λ) strikes on the dome surface, a portion of the fundamental light would interact with the TMD monolayer and convert into the backward SHG emission ($\lambda/2$) from the dome surface and forward SHG light emitted from the inner side of the TMD film. Simultaneously, the forward SHG and the remainder of fundamental light would impinge on the upper surface of bulk flake and get reflected, and then the reflected forward SHG would pass through the monolayer film while the reflected fundamental light will strike the film again and generate another forward SHG in the upward direction. During the process, if the height (h) between any site on the dome surface and the bottom can be converted to the path length difference equal to an odd multiple of $\lambda_{pump}/4$, all these SHG light waves would be in phase and undergo the constructive interference, generating a strong local emission [Fig. 1(c)]. In order to confirm this, AFM and SHG mapping measurements were performed on 3 individual domes which vary in size and intensity patterns [Fig. 1(d)]. Through extraction and comparison of the height and SHG intensity profiles of these domes, we found that these domes share a common aspect ratio ($h/R = 0.18$),[34] and the bright fringes can only exist when the domes' height exceeds around 160 nm. For the optical pattern of dome 1, the largest SHG is located at the center of the dome, as the height of dome 1 nears 160 nm. For those domes gradually larger than dome 1, the largest SHG emission area would transform from the central point to bright round fringes, with the relocation from the dome center to the location with separation heights of around 160 nm. The greatest SHG emission site would return to the center of the dome as the dome height increased, as was the case with dome 3 (whose height reached 260 nm). To determine the link between SHG intensity and dome height, the SHG intensity at the summit of many domes was extracted as shown in Fig. 1(e). It is clear to see that the SHG intensity would reach the maximum when the height is around 150 nm, then decline until the height was over 225 nm, at which point SHG intensity increased again. This was also the case for WS_2 domes (Fig. S1). This trend could be well described by an analytical solution based on a standing wave in the dome structure of the form

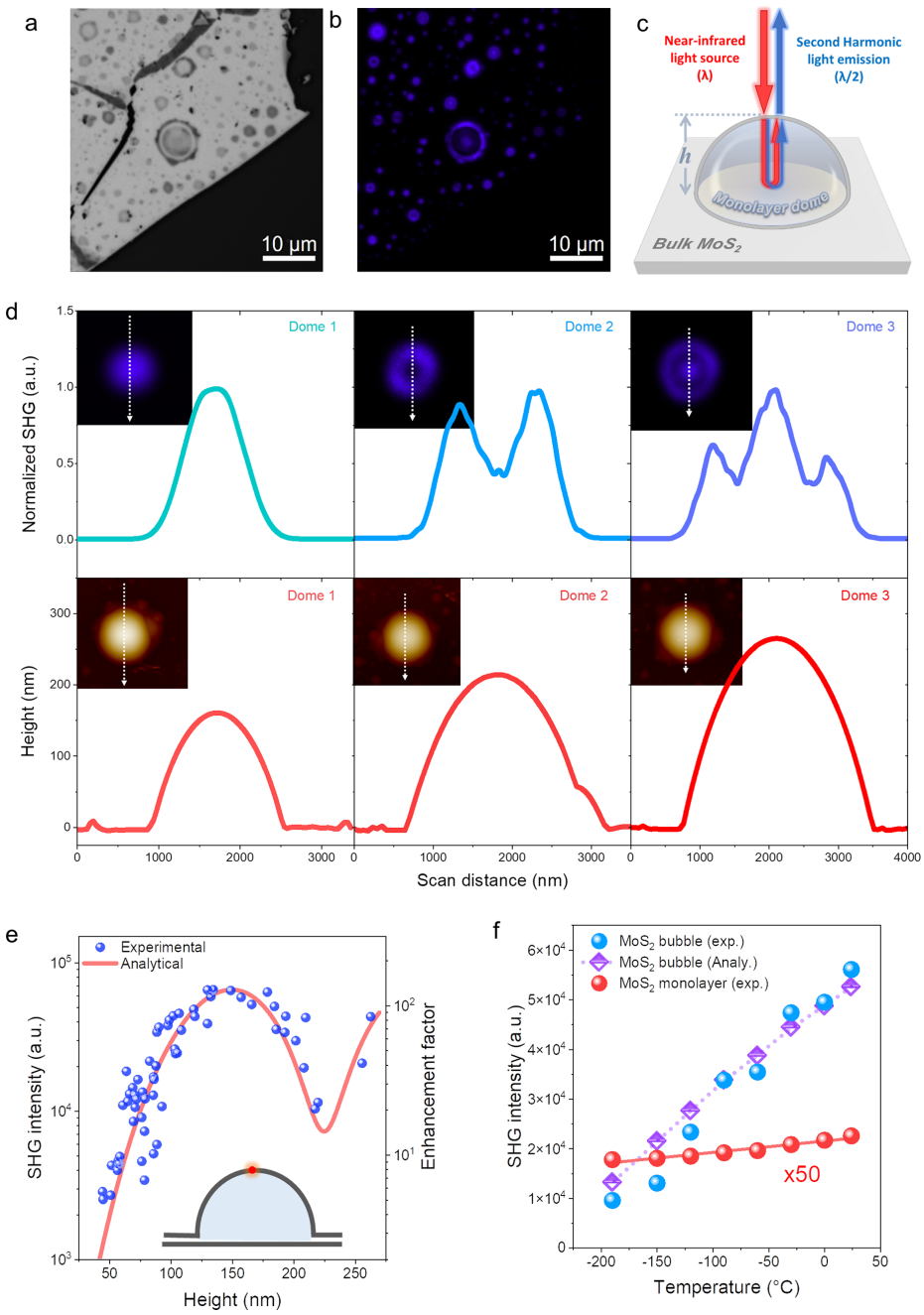

FIG. 1. Second harmonic optical response in MoS_2 pressurized domes. (a) Optical microscope image of pressurized domes formed on top of an MoS_2 flake. (b) Second harmonic generation (SHG) intensity mapping of the domes on the same flake shown in Fig. 1(a), the wavelength of the pump laser is 900 nm. Under the same excitation and collection conditions, monolayer (1L) domes exhibit the strongest SHG signal, whereas bilayer (2L) domes are invisible due to their centrosymmetric crystal orientation. (c) SHG mechanism in a ML dome. The red and blue wavy lines represent near infrared pump source and SHG output, respectively. (d) Extracted profile plots for different sized domes. Top panels display the normalized SHG intensity profile (purple) of the domes along the white dashed line of the SHG mapping image shown in the insets. Bottom panels: the measured height profile (red) of the corresponding domes along the white dashed line shown in insets obtained from atomic force microscope (AFM) images of each dome. (e) Experimental (blue spheres) SHG intensities collected at the top of domes (inset) as a function of dome's height. Analytical values (red line) match well with experimental results; right vertical axis: the enhancement factor of SHG compared with the 1L MoS_2 flake on SiO_2 (275 nm) substrate under the same excitation wavelength (900 nm) and power. (f) Temperature-dependent SHG measurements conducted on the 1L MoS_2 dome with 127 nm height (blue spheres) and the ML flake (red spheres), where the experimental SHG results obtained at different height induced by decreasing temperature have a good agreement with analytical SHG results in terms of dome height based on the RT condition (purple diamond).

$$I_{SH} \propto I_{pump} \cdot |(1+\rho_p e^{i2k_p h})^2 \cdot (1+\rho_{SH} e^{i4k_p h})|^2, \quad (1)$$

where h is the dome height, and $\rho_p = (1-n_p)/(1+n_p)$, $\rho_{SH} = (1-n_{SH})/(1+n_{SH})$ represent the reflection coefficient for the pump and SH lights, respectively, and n_p and n_{SH} are the refractive indices at pump and SH wavelengths, respectively. According to the analytical results, which shows great agreement with the numerical solution (Fig. S2), the SH intensity must have a strong dependence on the radial distance induced by the local height of the dome (separation distance), as this changes along the dome surface. Once the height of the dome reaches the critical value, the center would intermittently turn into the brightest emitter, accompanied by fringes as shown in Fig. 1(d). This is well supported by the patterns generated by the analytical method (Fig. S3), although there is minor discrepancy induced by the imaging resolution which cannot resolve more narrow fringes within the limited pixel lateral dimension. Thus, the optical pattern in Figs. 1(b) and 1(d) arises from constructive and destructive optical interference, which is also confirmed by the results of optical height obtained by phase shift interferometry (Fig. S4). Furthermore, even though the biaxial strain exerted on the dome samples would lead to a limited increase in the second order susceptibility $\chi^{(2)}$,[41] the constructive interference created by the local height of dome system is the dominant factor for the extraordinary SHG at the dome center, which enables 160 times enhancement compared to the monolayer MoS_2 flake on a 275 nm SiO_2 substrate. This enhancement factor is comparable to TMD monolayer flakes integrated into a photonic cavity device,[20] suggesting the great potential of TMD domes for future optical applications.

To further investigate the importance of the separation distance against total SH emission of the dome, temperature-dependent SHG measurements are carried out. When decreasing the environment temperature from room temperature (RT) to −190 °C, the SHG intensity of the dome declined by 83.4%, and this quenching factor was about 4 times larger than the value of a freestanding monolayer MoS_2 sample [21.1% shown in Fig. 1(f)]. This greater quenching factor is mainly due to the reduced dome volume (shrinking) because of the low temperature. The height of a dome is linearly proportional to temperature and decreased by ∼73% as the temperature dropped from RT to −190 °C. The same trend was also detected for WS_2 domes (Fig. S5). This proves that significant height variation would greatly affect phase matching for the constructive optical interference leading to exponential decay in total SH emission, in stark contrast to TMD monolayer flakes whose SHG intensity changes linearly with modifying lattice dimensions induced by thermal expansion.[42] Moreover, based on the assumption of a constant aspect ratio ($h/R = 0.18$) of domes with temperatures and the estimation of the dome height at different temperature, the comparison between the experimental result of temperature-dependent SHG and analytical results at corresponding height values exhibited a good consistency. This directly further proves that the separation distance in the dome system plays the dominant role in dramatic SH emission changes. It is worth noting that despite the substantial intensity fall for the SH emission in the dome at low temperatures, the absolute SH intensity of the dome is still significantly higher than that of the monolayer flake.

Such robust enhancement observed in TMD monolayer domes enable them to become high-conversion-efficiency light emitters, which may have profound implications for future nonlinear optical devices such as quantum photonics and optical parametric generation (OPG).[43] Meanwhile, the large size and hemi-spherical geometry of domes can serve as a non-bleaching optical probe offering outstanding up and down conversion fluorescent capability,[44–46] demonstrating great potential for future biomedical diagnostic and imaging applications even in the extreme conditions.

Polarization-dependent SHG on biaxial strain

Polarization-dependent SHG is an effective technique to identify and resolve lattice distortion, as the strain would modulate the second-order nonlinear susceptibility tensor $\chi^{(2)}_{ijk}$ and break the symmetry in the SHG polarization pattern.[47] Pressurized TMD domes are a promising candidate for SHG studies, linking complex strain components to nonlinear optical properties. In addition to the enhanced intensity and predictable locations of SHG fringes brought on by the optical interference, the domes also have differing strain components in both magnitude and orientation directions that heavily influence SHG. Here, polarization-dependent SHG measurements were conducted at multiple locations to investigate the permanent biaxial strain in circumferential and radial directions (θ_h and θ_r) exerted on the pressurized TMD domes, where θ_r is equivalent to the azimuthal angle with respect to the center of the dome and is perpendicular to θ_h.

Since domes are formed by the competition between internal gas pressure, elastic energy, and van der Waals adhesion energy of the TMD film,[36,48] there is a divergent strain field over the dome surface. When moving away from the dome summit toward the edge, the biaxial strain is radially distributed and finally results in uniaxial strain from the center to the edge of the dome,[32,34,35] ranging from around 5% to 2% as determined by the methods in SI Note 1 and demonstrated in Fig. S6(a). The strain variation is further confirmed by the phonon mode shifts depicted in location-dependent Raman spectra (Fig. S7, supplementary material Note 2). To investigate the influence of the bi-axial strain magnitudes on the lattice distortion, multiple sites were examined from the top toward the bottom of the dome. For simplicity, like the coordinates on earth which can be described by latitude and longitude, test sites on the TMD dome can also be determined by the orientation of the radial strain component, θ_r and the ratio of radial distance from dome center, r/R. Locations at $r/R = 0$, 0.16, 0.26, 0.32, and 0.39 in a certain radial direction ($\theta_r = 20°$) were selected [Fig. S6(b)], whose decreasing trend of the total strain is also confirmed by blueshifts in PL and Raman spectra extracted at those corresponding locations [Figs. S8(a) and 8(b)]. The corresponding experimental SHG polar patterns under the application of various levels of biaxial strain are depicted in Figs. 2(a)–2(e). When the examined site was at the top of the dome, equal bi-axial strain components ($\varepsilon_r = \varepsilon_h$) exist, and the lattice would be stretched with the same displacement. The corresponding SHG polar pattern, thus, would remain the same shape as in unstrained flakes,[15,33,49] featuring six uniform petals [Fig. 2(a)]. However, with locations away from the top of the dome, the uneven biaxial strain leads to distorted patterns, and the size of petals, i.e., anisotropic SH response, is influenced and manipulated by the ratio between the two strain components [Figs. 2(b)–2(e)]. As the radial distance increases, the relative weight of ε_r on the total biaxial strain becomes greater; therefore, the overall pattern shape is reduced in θ_h and elongated in θ_r [Fig. 2(e)], indicating the differing in-plane displacement of Mo and S atoms sustained via different levels of strain components.[30]

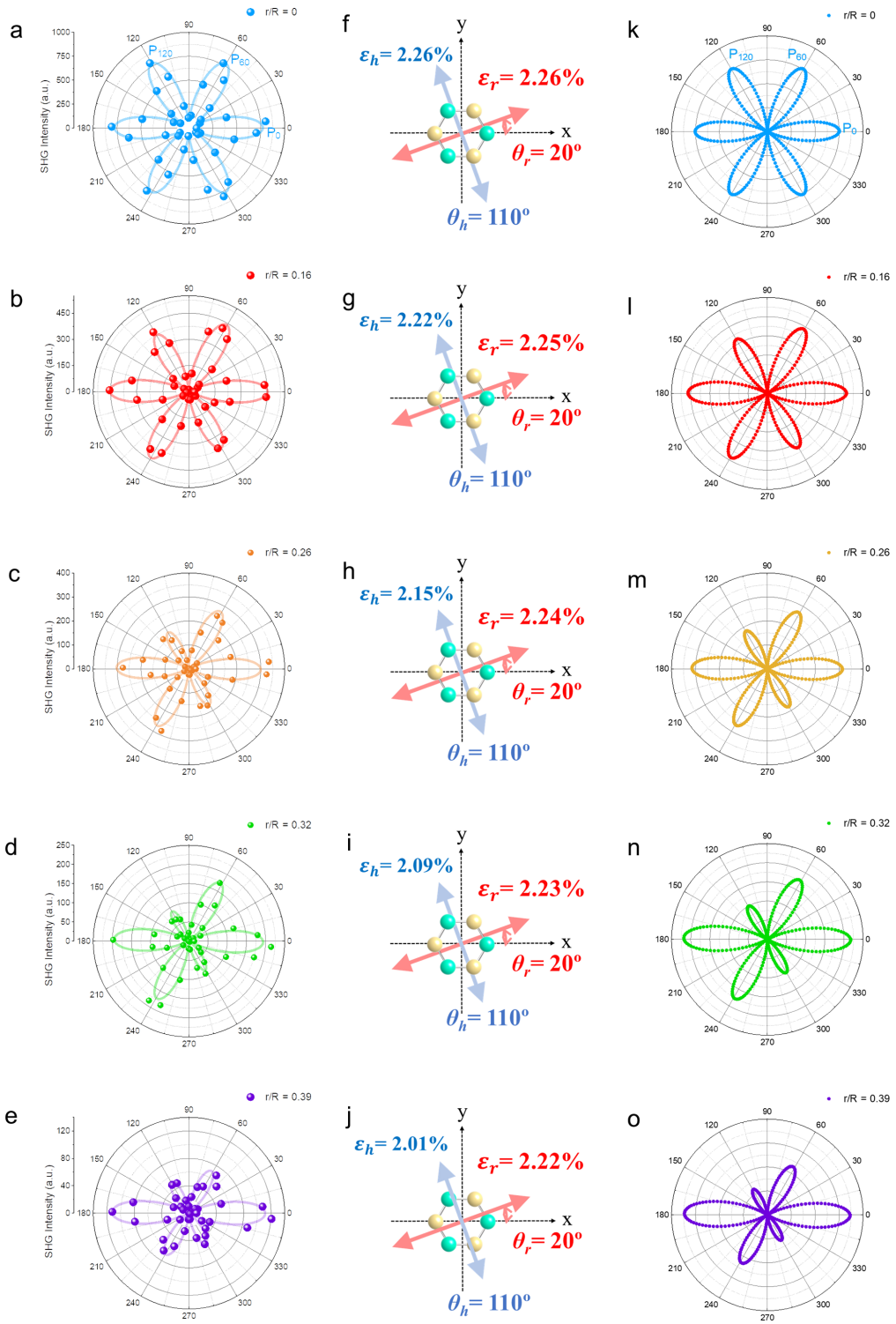

FIG. 2. Probing the anisotropic SH response with the evolution of the lattice distortion induced by varying biaxial strain magnitudes. (a)–(e) Polarization-resolved SHG measured experimentally with varied levels of strain in the same θ_r (f)–(j) Schematic illustrations of the strain conditions at various sites distant from the dome's center from the top view, where the values of ε_r (red arrow) and ε_h (blue arrow) change with the radius in the same principal orientation of the radial strain, $\theta_r = 20°$. (k)–(o) Analytical results of polarization-resolved SHG at different sites with the corresponding strain magnitudes in the same direction as shown in (f)–(j), respectively.

To understand SHG polar pattern evolution and the involved photoelastic effect, an established approach was employed for the analytical SHG polar pattern evolution under strain. The parallel polarized SHG intensity "$I_{//}(2\omega)$" under bi-axial strain for D_{3h} symmetry class considering the photoelastic effect has the form[50]

$$I_{//}(2\omega) \propto \frac{1}{4}[A\cos(3\phi - 3\delta) + B\cos(2\theta_r + \phi - 3\delta)]^2, \quad (2)$$

where $A = (1-\nu)(p_1+p_2)(\varepsilon_r+\varepsilon_h) + 2\chi_0^{(2)}$ and $B = (1+\nu)(p_1 - p_2)(\varepsilon_r - \varepsilon_h)$, p_1 and p_2 are the photoelastic coefficients, ν is Poisson's ratio, θ_r is radial strain direction, ϕ is the polarization angle, δ is the armchair direction and $\chi_0^{(2)}$ is the nonlinear susceptibility parameter of the unstrained crystal lattice. The strain conditions at the investigated sites were determined [Eqs. (S2) and (S3)] by taking advantage of the universal h/R ratio and the corresponding radial distances r/R of the sites (supplementary material Note 1). Hence, the strain conditions (ε_r, ε_h, and θ_r) at corresponding test sites, as indicated in Fig. S6(b), are interpreted as (2.26%, 2.26%, 20°), (2.25%, 2.22%, 20°), (2.4%, 2.15%, 20°), (2.23%, 2.09%, 20°), and (2.22%, 2.01%, 20°), respectively. According to these values, the analytical polar patterns were subsequently generated, and they displayed the same trend in lattice distortion as described in the evolution of the pattern shape with locations. The plots at the top of the dome have a uniform sixfold rotational symmetry, while plots with breaking symmetry induced by the lattice distortion were found in the other locations aside from the center [Figs. 2(k)–2(o)], which has a great agreement with the experimental data. Therefore, considering the strain ratios in specific orientations, larger petals correspond to the larger strain level and minimum angle difference between θ_r and armchair direction δ of the lattice, while the less strained direction would lead to shrunken petals. Unlike the case of uniaxial strain, the local lattice is not significantly distorted despite the large amount of total strain applied.[30,33,50]

Moreover, as the strain magnitudes are directly related to the coordinates on the dome surface, locations with the same radial distance away from the center of the dome are supposed to share the same strain magnitudes. To further monitor the lattice distortion in various directions, polarization-dependent measurements were conducted in a circumferential direction on the surface of the dome. For convenient positioning and measurement, the test sites were selected along a bright fringe circle of a monolayer dome sample. The armchair direction δ of the dome sample was initially aligned with the horizontal direction (x axis), so the orientations of ε_r are equivalent to the azimuthal angles of test sites as shown in Fig. S6(c), leading to multi-angular strain components with the same magnitude. In Figs. 3(a)–3(e), the SHG polar plots were experimentally obtained from test sites with azimuthal angles of 30°, 60°, 90°, 120°, and 150°. The distorted sixfold SHG patterns indicate that biaxial strain with uneven components exist at these sites, and each site withstood the same magnitude of total strain as indicated by the corresponding PL and Raman spectra in Figs. S8(c) and S8(d). In addition, the varying orientations of biaxial strain applied were clearly interpreted as differing petal sizes at each site. According to the plots, there are two groups containing identical shapes of petal patterns. The first group is the shape containing one pair of petals having the largest size, and the other two pairs of small petals having smaller and similar sizes [Figs. 3(b) and 3(d)]. When θ_r is parallel to a certain δ, the stronger tension effectively pulls the Mo and S atoms, resulting in the larger ε_r. Simultaneously, the weaker circumferential tension at the middle of the remaining two δ directions results in the minor in-plane displacement of covalent bonds and the reduced ε_h. This allows the SHG polar plots to only possess one pair of the largest petals. The second group is where two pairs of larger petals shared similar sizes as indicated in Figs. 3(a), 3(c), and 3(e). This behavior arises from the stronger ε_r applied at the mid-point between atoms, when θ_r was equal to the average angle value of the other two δ. During the transition of ε_r applied closer to either the S or Mo atom, one of two pairs of large petals shrinks, but another pair expands, indicating the θ_r approaches the bigger petal's δ (Fig. S9). This is also demonstrated by the patterns in Fig. 2, where the orientation of ε_r was close to δ at 30°. Therefore, owing to the interaction between strain orientation and D_{3h} symmetry in monolayer TMD materials, the lattice undergoes periodic distortion and transformation, demonstrated by the same polar patterns with 60° rotation.

As in the section Results and Discussion, the multi-angular strain conditions of $\varepsilon_r = 2.19\%$, and $\varepsilon_h = 1.89\%$ [Figs. 3(f)–3(j)] could also be easily estimated [Eqs. (S2) and (S3) in supplementary material Note 1] and the r/R obtained by comparing the radius values of the bright fringe and the footprint radius of dome. Taking advantage of the strain conditions, Figs. 3(k)–3(o) present the corresponding analytical SHG polar patterns governed by Eq. (2), all of which have great agreement with the experimental patterns in terms of the pattern shape and rotation period. Some minor discrepancy could be attributed to the variation in strain magnitudes arisen from the ideal and actual dome geometries, as tiny side domes form around the boundary of the examined dome, which may deviate the actual shape from the circular round shape (Fig. S10).[34] Overall, the analytical solution confirms that with θ changing, the petal size and pattern shapes would periodically restore during this process, as the indication of the interaction between the mechanical tension and TMD lattice structure.

For a better visualization of the changes in the anisotropic SHG response for varying biaxial strain conditions, Fig. 4 presents a contour plot describing the evolution of the polar plots induced by strain orientations and the relative weight ratio of strain components. We measure the SH response of the atoms parallel to the horizontal axis (size of petal lying at 0°, P_0) and then monitor its changes when comparing it with the overall response values ($P_0 + P_{60} + P_{120}$) of atoms laying in three axes at 0°, 60°, and 120°, as indicated in Figs. 2, 3(a), and 3(k). The two extremes (0.042 and 0.72) of $P_0/(P_0 + P_{60} + P_{120})$ could be found when the strain ratio $\varepsilon_h/\varepsilon_r = 0$ and the principal $\theta_r = 90°$ and 0°, respectively. Accordingly, when the biaxial strain situation is close to that of uniaxial strain, it may result in greater lattice distortion as indicated by the increased slope and amplitude of the wave.[30,31] On the other hand, when the biaxial strain is nearly isotropic, the polar shape exhibits a uniform sixfold symmetry regardless of the strain orientation as seen by the flattening of the curve, which has great consistency and agreement with the experimental results.[50] Similar results were also found regarding the strain difference between biaxial components (Fig. S11). Therefore, this could be used as a quick tool to identify the existence of possible biaxial strain in different scenarios and to resolve its ratio and directions by applying polarization-dependent SHG measurement and observing one petal compared to others.

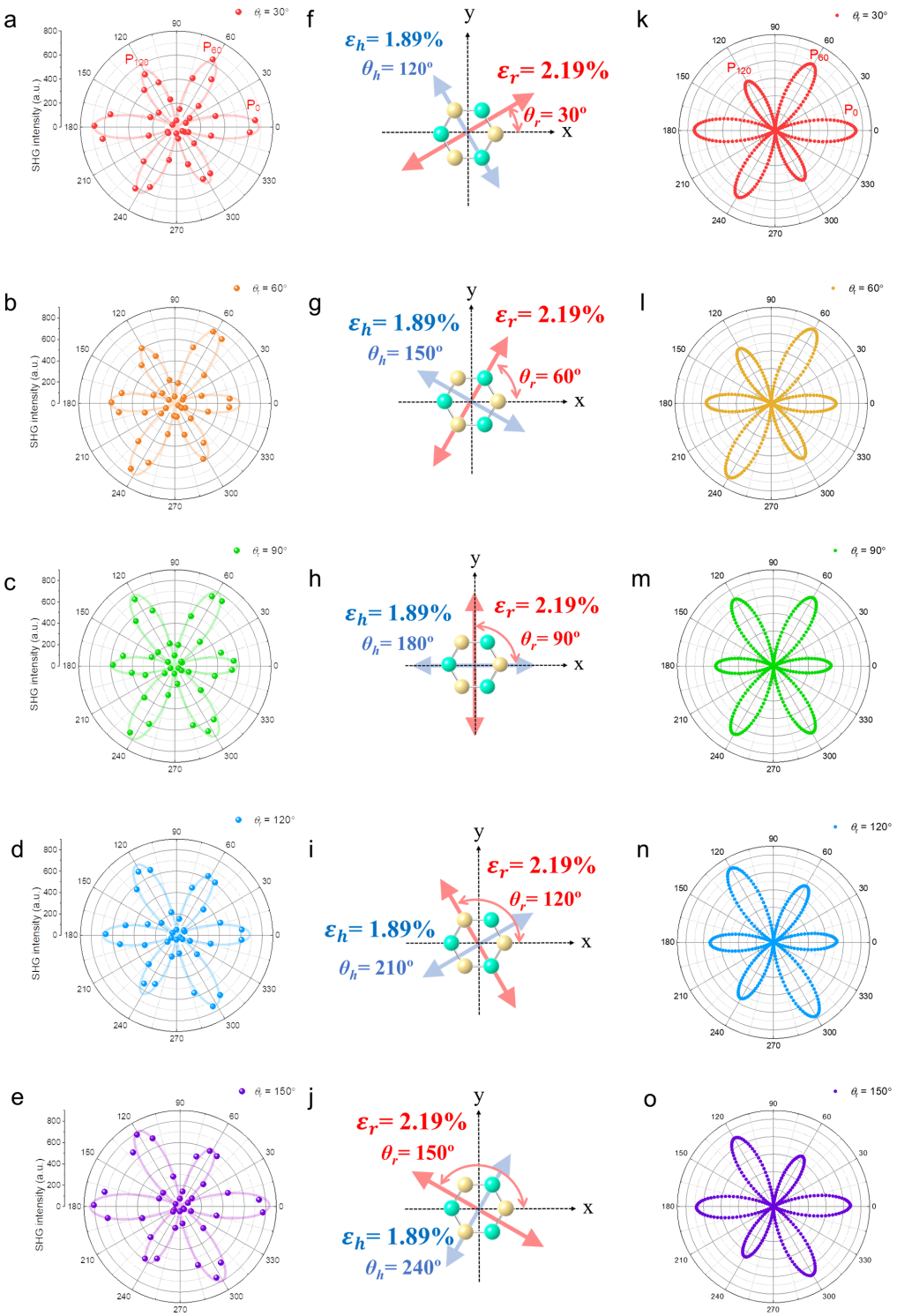

FIG. 3. Probing the anisotropic SH response with the evolution of the lattice distortion induced by varying biaxial strain orientations. (a)–(e) Experimental polarization-resolved SHG measured at the locations shown with different radial strain orientations but with the same magnitude. (f)–(j) Schematics of the strain conditions at the locations along a hoop of the dome, which are represented as arrows with the values of radial (ε_r, red arrow) and circumferential (ε_h, blue arrow) strains applied in various radial directions (30°–150°). **(k-o)** Analytical results of polarization-resolved SHG employed with the corresponding strain conditions in relation to the sites on the dome structure in (f)–(j).

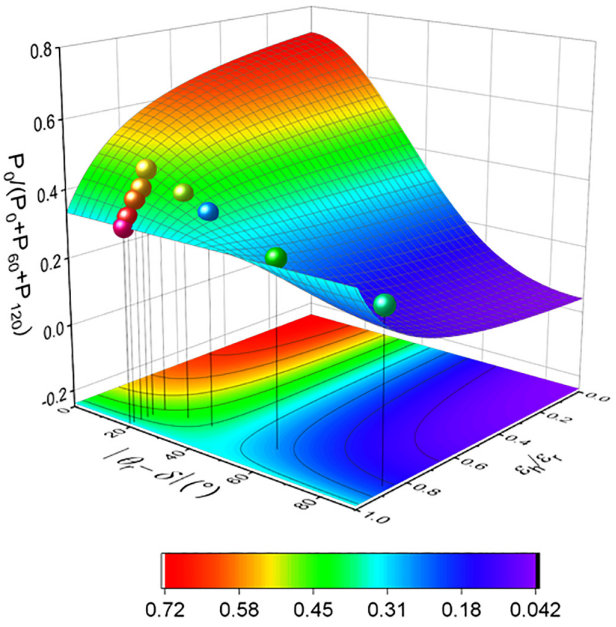

FIG. 4. Contour map showing the evolution of SHG polar pattern regarding strain ratio ($\varepsilon_h/\varepsilon_r$) and principal strain orientation ($\theta_r - \delta$). $P_0/(P_0 + P_{60} + P_{120})$ represents the variation in the sizes of petals located at 0°, 60°, and 120°. The values extracted from experimental SHG polar patterns are indicated by the spheres, and contour map is converted by the analytical patterns, both of which have great consistency under various strain conditions.

CONCLUSION

In conclusion, we have shown extraordinary SHG emission in TMD domes, exploiting this inherent feature to investigate the influence of biaxial strain vs the anisotropic SHG response. Owing to the distinct separation distance induced by the encapsulated pressurized hydrogen gas, TMD domes serve as the hemi-spherical optical resonator and possess internal in-phase interference, which can effectively achieve the enhanced light-matter interaction length and extraordinary increase in SHG emission. Therefore, the SHG magnitude enhancement is improved by 160 times in ambient condition and even remains robust in low temperature environments having at least 1 order of magnitude enhancement. It exhibits a promising approach to realize the effective enhancement in other nonlinear optical performance like third harmonic generation (THG) and four wave mixing (FWM). Moreover, polarization-dependent SHG was employed to comprehensively map anisotropic response induced by varying biaxial strain components over a diverging strain field in radial and circumferential directions. The results demonstrate that the anisotropic response of TMD films is less sensitive to the application of biaxial strain, as depicted by the less distorted polar plots, although the total magnitude of biaxial strain could be much larger than that of uniaxial strain. Our findings lay a strong foundation for the quick detection of possible anisotropic deformation in 2D materials and pave a promising path toward the realization of strain-engineered nonlinear optics with modest polarization selectivity for future quantum photonics and biomedical imaging and sensing devices.

Experimental methods

Sample fabrication

Thick TMD flakes were mechanically exfoliated onto SiO_2/Si (275 nm SiO_2), and then the samples were mounted in the vacuum chamber followed by low-energy proton irradiation in high vacuum condition. Meanwhile, within the ionization chamber, protons were produced and then accelerated by a grid system to produce an H^+ beam flushing the sample surface with low energies (between 5 and 20 eV). When target dose of protons was achieved, the treatment process completed and pressurized domes formed successfully, with the dose being determined by the treatment time and flux.

Optical characterizations

Optical microscopic images were taken by a Zeiss 780 confocal microscope equipped with 633 nm single photon laser. SHG measurements are performed on Zeiss 780 Confocal Microscopy. The fundamental laser field is provided tunable pulse laser Ti:Sapphire laser with a pulse width of 150 fs and a repetition rate of 80 MHz. The sample was excited and measured under a 50× confocal objective lens (NA = 0.85), and the results were collected in the reflection mode at a fundamental laser wavelength of 900 nm. During the measurements, the power of excitation light would be kept below 1 μW to avoid possible heating influence on the internal pressure and volume of the tested dome, ensuring the collected data with higher accuracy. An analyzer (polarizer) was used for polarization-resolved SHG to choose the SH radiation's polarization component, parallel to the polarization of the pump beam whose wavelength was set at 900 nm. The sample was placed on a rotational stage to collect the SH response in terms of polarization angles. Zeiss 780 confocal microscopy completes all tests and imaging for optical characterization measurements, where the high imaging resolution (pixel size = 0.03 μm) is used to capture more emission details of dome samples than the relatively low resolution (Fig. S12). All data were processed and analyzed by image processing software, Zen 3.4 (blue edition). Surface profiler (Veeco NT9100) employed with a 533 nm laser was used to obtain all the optical path length (OPL) values for dome samples in PSI mode.

Atomic force microscope measurement

The AFM measurements were captured using a Bruker Dimension Icon AFM. The topographic images, height profile, and the aspect ratio of the domes were obtained in Scanasyst air experiment mode with soft cantilevers, Scanasyst-Air, whose nominal spring constant k and nominal tip radius are 0.4 N/m and 2 nm, respectively.

SUPPLEMENTARY MATERIAL

See the supplementary material for details. All additional data and supplementary material regarding optical interference in dome, Raman results, and polarization-dependent SHG results are presented in the supplementary material file.

ACKNOWLEDGMENTS

We would like to thank the technical support of Mr. D. Webb from the Centre of Advanced Microscopy (CAM), Australian National University. We acknowledge the support from the funding

support from ANU Ph.D. student scholarship, Australian Research Council (ARC; Nos. DE140100805 and DP180103238), Australian National Heart Foundation (ARIES ID: 35852), European Union's Horizon 2020 research and innovation program (QuantERA II Program, Grant Agreement No. 101017733) with funding organizations Ministero dell'Universitá e della Ricerca (MUR) and Consiglio Nazionale delle Ricerche (CNR).

AUTHOR DECLARATIONS

Conflict of Interest

The authors have no conflicts to disclose.

Author Contributions

Boqing Liu: Formal analysis (lead); Investigation (lead); Methodology (lead); Writing – original draft (lead). **Antonio Polimeni:** Supervision (equal); Writing – review & editing (equal). **Yuerui Lu:** Supervision (equal); Writing – review & editing (equal). **Tanju Yildirim:** Writing – original draft (supporting); Writing – review & editing (supporting). **Elena Blundo:** Investigation (supporting); Methodology (supporting); Writing – review & editing (supporting). **Domenico de Ceglia:** Investigation (supporting); Writing – review & editing (supporting). **Ahmed Raza Khan:** Investigation (supporting); Writing – review & editing (supporting). **Zongyou Yin:** Investigation (supporting); Supervision (supporting). **Hieu Nguyen:** Writing – review & editing (supporting). **Giorgio Pettinari:** Writing – review & editing (supporting). **Marco Felici:** Methodology (supporting).

DATA AVAILABILITY

The data that support the findings of this study are available from the corresponding authors upon reasonable request.

REFERENCES

[1]T. Helk, E. Berger, S. Jamnuch, L. Hoffmann, A. Kabacinski, J. Gautier, F. Tissandier, J.-P. Goddet, H.-T. Chang, J. Oh, C. D. Pemmaraju, T. A. Pascal, S. Sebban, C. Spielmann, and M. Zuerch, Sci. Adv. **7**(21), eabe2265 (2021).
[2]S. Shwartz, M. Fuchs, J. B. Hastings, Y. Inubushi, T. Ishikawa, T. Katayama, D. A. Reis, T. Sato, K. Tono, M. Yabashi, S. Yudovich, and S. E. Harris, Phys. Rev. Lett. **112**(16), 163901 (2014).
[3]T. Manaka, E. Lim, R. Tamura, and M. Iwamoto, Nat. Photonics **1**(10), 581–584 (2007).
[4]A. E. Willner, S. Khaleghi, M. R. Chitgarha, and O. F. Yilmaz, J. Lightwave Technol. **32**(4), 660–680 (2014).
[5]R. Trebino, K. W. DeLong, D. N. Fittinghoff, J. N. Sweetser, M. A. Krumbügel, B. A. Richman, and D. J. Kane, Rev. Sci. Instrum. **68**(9), 3277–3295 (1997).
[6]G. Wang, X. Marie, I. Gerber, T. Amand, D. Lagarde, L. Bouet, M. Vidal, A. Balocchi, and B. Urbaszek, Phys. Rev. Lett. **114**(9), 097403 (2015).
[7]Z. Ye, T. Cao, K. O'Brien, H. Zhu, X. Yin, Y. Wang, S. G. Louie, and X. Zhang, Nature **513**(7517), 214–218 (2014).
[8]W.-T. Hsu, Z.-A. Zhao, L.-J. Li, C.-H. Chen, M.-H. Chiu, P.-S. Chang, Y.-C. Chou, and W.-H. Chang, ACS Nano **8**(3), 2951–2958 (2014).
[9]C. Jin, E. C. Regan, A. Yan, M. Iqbal Bakti Utama, D. Wang, S. Zhao, Y. Qin, S. Yang, Z. Zheng, S. Shi, K. Watanabe, T. Taniguchi, S. Tongay, A. Zettl, and F. Wang, Nature **567**(7746), 76–80 (2019).
[10]J. Y. Chauleau, E. Haltz, C. Carrétéro, S. Fusil, and M. Viret, Nat. Mater. **16**(8), 803–807 (2017).
[11]K.-Q. Lin, S. Bange, and J. M. Lupton, Nat. Phys. **15**(3), 242–246 (2019).
[12]Y. Wang, J. Xiao, S. Yang, Y. Wang, and X. Zhang, Opt. Mater. Express **9**(3), 1136–1149 (2019).
[13]W. Wu, L. Wang, Y. Li, F. Zhang, L. Lin, S. Niu, D. Chenet, X. Zhang, Y. Hao, T. F. Heinz, J. Hone, and Z. L. Wang, Nature **514**(7523), 470–474 (2014).
[14]L. M. Malard, T. V. Alencar, A. P. M. Barboza, K. F. Mak, and A. M. de Paula, Phys. Rev. B **87**(20), 201401 (2013).
[15]N. Kumar, S. Najmaei, Q. Cui, F. Ceballos, P. M. Ajayan, J. Lou, and H. Zhao, Phys. Rev. B **87**(16), 161403 (2013).
[16]A. Castellanos-Gomez, R. Roldán, E. Cappelluti, M. Buscema, F. Guinea, H. S. J. van der Zant, and G. A. Steele, Nano Lett. **13**(11), 5361–5366 (2013).
[17]S. Bertolazzi, J. Brivio, and A. Kis, ACS Nano **5**(12), 9703–9709 (2011).
[18]A. Falin, M. Holwill, H. Lv, W. Gan, J. Cheng, R. Zhang, D. Qian, M. R. Barnett, E. J. G. Santos, K. S. Novoselov, T. Tao, X. Wu, and L. H. Li, ACS Nano **15**(2), 2600–2610 (2021).
[19]E. Blundo, C. Di Giorgio, G. Pettinari, T. Yildirim, M. Felici, Y. Lu, F. Bobba, and A. Polimeni, Adv. Mater. Interfaces **7**(17), 2000621 (2020).
[20]T. K. Fryett, K. L. Seyler, J. Zheng, C.-H. Liu, X. Xu, and A. Majumdar, 2D Mater. **4**(1), 015031 (2016).
[21]R. Trivedi, U. K. Khankhoje, and A. Majumdar, Phys. Rev. Appl. **5**(5), 054001 (2016).
[22]A. R. Khan, L. Zhang, K. Ishfaq, A. Ikram, T. Yildrim, B. Liu, S. Rahman, and Y. Lu, Adv. Funct. Mater. **32**(3), 2105259 (2021).
[23]K. L. Seyler, J. R. Schaibley, P. Gong, P. Rivera, A. M. Jones, S. Wu, J. Yan, D. G. Mandrus, W. Yao, and X. Xu, Nat. Nanotechnol. **10**(5), 407–411 (2015).
[24]E. Blundo, E. Cappelluti, M. Felici, G. Pettinari, and A. Polimeni, Appl. Phys. Rev. **8**(2), 021318 (2021).
[25]K. He, C. Poole, K. F. Mak, and J. Shan, Nano Lett. **13**(6), 2931–2936 (2013).
[26]H. J. Conley, B. Wang, J. I. Ziegler, R. F. Haglund, S. T. Pantelides, and K. I. Bolotin, Nano Lett. **13**(8), 3626–3630 (2013).
[27]T. T. Tran, K. Bray, M. J. Ford, M. Toth, and I. Aharonovich, Nat. Nanotechnol. **11**(1), 37–41 (2016).
[28]H. Moon, G. Grosso, C. Chakraborty, C. Peng, T. Taniguchi, K. Watanabe, and D. Englund, Nano Lett. **20**(9), 6791–6797 (2020).
[29]L. Mennel, V. Smejkal, L. Linhart, J. Burgdörfer, F. Libisch, and T. Mueller, Nano Lett. **20**(6), 4242–4248 (2020).
[30]J. Liang, J. Zhang, Z. Li, H. Hong, J. Wang, Z. Zhang, X. Zhou, R. Qiao, J. Xu, P. Gao, Z. Liu, Z. Liu, Z. Sun, S. Meng, K. Liu, and D. Yu, Nano Lett. **17**(12), 7539–7543 (2017).
[31]A. R. Khan, B. Liu, T. Lu, L. Zhang, A. Sharma, Y. Zhu, W. Ma, and Y. Lu, ACS Nano **14**(11), 15806–15815 (2020).
[32]E. Blundo, T. Yildirim, G. Pettinari, and A. Polimeni, Phys. Rev. Lett. **127**(4), 046101 (2021).
[33]L. Mennel, M. M. Furchi, S. Wachter, M. Paur, D. K. Polyushkin, and T. Mueller, Nat. Commun. **9**(1), 516 (2018).
[34]D. Tedeschi, E. Blundo, M. Felici, G. Pettinari, B. Liu, T. Yildrim, E. Petroni, C. Zhang, Y. Zhu, and S. Sennato, Adv. Mater. **31**(44), 1903795 (2019).
[35]Z. Dai, Y. Hou, D. A. Sanchez, G. Wang, C. J. Brennan, Z. Zhang, L. Liu, and N. Lu, Phys. Rev. Lett. **121**(26), 266101 (2018).
[36]D. Lloyd, X. Liu, N. Boddeti, L. Cantley, R. Long, M. L. Dunn, and J. S. Bunch, Nano Lett. **17**(9), 5329–5334 (2017).
[37]E. Khestanova, F. Guinea, L. Fumagalli, A. K. Geim, and I. V. Grigorieva, Nat. Commun. **7**, 12587 (2016).
[38]B. Liu, T. Yildirim, T. Lü, E. Blundo, L. Wang, L. Jiang, H. Zou, L. Zhang, H. Zhao, Z. Yin, F. Tian, A. Polimeni, and Y. Lu, Nat. Commun. **14**(1), 1050 (2023).
[39]E. Blundo, M. Felici, T. Yildirim, G. Pettinari, D. Tedeschi, A. Miriametro, B. Liu, W. Ma, Y. Lu, and A. Polimeni, Phys. Rev. Res. **2**(1), 012024 (2020).
[40]T. P. Darlington, C. Carmesin, M. Florian, E. Yanev, O. Ajayi, J. Ardelean, D. A. Rhodes, A. Ghiotto, A. Krayev, K. Watanabe, T. Taniguchi, J. W. Kysar, A. N. Pasupathy, J. C. Hone, F. Jahnke, N. J. Borys, and P. J. Schuck, Nat. Nanotechnol. **15**(10), 854–860 (2020).
[41]K. Beach, M. C. Lucking, and H. Terrones, Phys. Rev. B **101**(15), 155431 (2020).
[42]A. R. Khan, B. Liu, L. Zhang, Y. Zhu, X. He, L. Zhang, T. Lü, and Y. Lu, Adv. Opt. Mater. **8**(17), 2000441 (2020).
[43]A. Ciattoni, A. Marini, C. Rizza, and C. Conti, Light **7**(1), 5 (2018).
[44]A. Pramanik, S. R. Chavva, Z. Fan, S. S. Sinha, B. P. Nellore, and P. C. Ray, J. Phys. Chem. Lett. **5**(12), 2150–2154 (2014).

[45]J. L. Li, H. C. Bao, X. L. Hou, L. Sun, X. G. Wang, and M. Gu, Angew. Chem., Int. Ed. **51**(8), 1830–1834 (2012).
[46]H. Dong, S. Tang, Y. Hao, H. Yu, W. Dai, G. Zhao, Y. Cao, H. Lu, X. Zhang, and H. Ju, ACS Appl. Mater. Interfaces **8**(5), 3107–3114 (2016).
[47]I. L. Lyubchanskii, N. N. Dadoenkova, M. I. Lyubchanskii, T. Rasing, J.-W. Jeong, and S.-C. Shin, Appl. Phys. Lett. **76**(14), 1848–1850 (2000).
[48]S. P. Koenig, N. G. Boddeti, M. L. Dunn, and J. S. Bunch, Nat. Nanotechnol. **6**, 543 (2011).
[49]Y. Li, Y. Rao, K. F. Mak, Y. You, S. Wang, C. R. Dean, and T. F. Heinz, Nano Lett. **13**(7), 3329–3333 (2013).
[50]L. Mennel, M. Paur, and T. Mueller, APL Photonics **4**(3), 034404 (2019).

Supplementary information

Extraordinary Second Harmonic Generation modulated by Divergent Strain Field in Pressurized Monolayer Domes

Boqing Liu[1], Tanju Yildirim[2], Elena Blundo[3], Domenico de Ceglia[4], Ahmed Raza Khan[1], Zongyou Yin[5], Hieu T. Nguyen[1], Giorgio Pettinari[3], Marco Felici[3], Antonio Polimeni[3*], Yuerui Lu[1,6*]

[1]School of Engineering, College of Engineering, Computing and Cybernetics, The Australian National University, Canberra ACT, 2601, Australia

[2]Center for Functional Sensor & Actuator (CFSN), Research Center for Functional Materials, National Institute for Materials Science (NIMS), 1-1 Namiki, Tsukuba, Ibaraki 305-0044, Japan

[3]Dipartimento di Fisica Sapienza Università di Roma, Roma 00185, Italy

[4]Department of Information Engineering, University of Brescia, Brescia 25121, Italy

[5]Research School of Chemistry, College of Science, The Australian National University, Canberra, ACT 2601, Australia

[6]ARC Centre of Excellence in Quantum Computation and Communication Technology ANU node, Canberra, ACT 2601, Australia

*To whom correspondence should be addressed: Yuerui Lu (yuerui.lu@anu.edu.au) and Antonio Polimeni (antonio.polimeni@uniroma1.it)

Note 1: Strain distribution over the dome

The first step in determining the magnitude of strain and its components is to comprehend the dome profiles. Thus, the experimental profile was well described by the unified power form given as (Fig. 2a)[1, 2]

$$h(r) = h_0\left[1 - \left(\frac{r}{R}\right)^q\right], \tag{1}$$

where q represents the curvature factor, h and h_0 are the separation height and the dome central height, R is the dome footprint radius and r is the radial position along the footprint radius. The statistical analysis of dome profiles suggested that the aspect ratio $h_0/R \approx 0.18$ and $q \approx 2.1$ were universal and independent of dome sizes, so the shape of the domes can be described as universal. The strain components and the distribution on the dome could be subsequently classified into radial (ε_r) and circumferential (ε_h) directions, see inset in Fig. 2a, and are a function of r[1, 2]:

$$\varepsilon_r(r) = f(v,q)\left(\frac{h_0}{R}\right)^2\left[1 - g(v,q)\left(\frac{r}{R}\right)^{2q-2}\right],$$

$$\varepsilon_h(r) = f(v,q)\left(\frac{h_0}{R}\right)^2\left[1 - \left(\frac{r}{R}\right)^{2q-2}\right], \tag{2}$$

where $f(v,g)$ and $g(v,g)$ are functions of v, the Poisson's ratio and curvature factor q[1, 2] given by

$$f(v,q) = \left(\frac{q}{8}\right)\left[\frac{2q-1-v}{q-1}\right],$$

$$g(v,q) = \frac{1+v+2qv}{2q-1-v}. \tag{3}$$

Hence referring to Eq. 2, the aspect ratio (h_0/R) can determine the maximum strain of domes while the q plays an important role in determination of strain distribution. As shown in Fig. S6a, for a typical dome with h_0/R = 0.18, the equal biaxial ($\varepsilon_r = \varepsilon_h$) is exerted at the center (r = 0, $h = h_0$), creating a total strain around 4.57%, but this value gradually declines when approaching the edges ($r = R$), which is also confirmed by the peak shifts in Raman measurements (Figure. S7)[3-6]. In this process, the biaxial strain condition eventually turned into the uniaxial one, because the ε_h component would eventually vanish at the edge whereas ε_r dropped from 2.28% to 2.13% with a neglectable decrement.

As the strain is unevenly distributed over the entire surface of the dome, strain components at the locations with same h and r remain have constant magnitudes but have varying orientations with respect to the lattice orientation. Like traveling on earth planet along a certain longitude or latitude line enables distinct changes in temperature or time zones. The dome structure enables us to investigate the evolution of lattice distortions under strain with differing conditions at different locations along the radial and circumferential directions. Figure S6b elaborates 5 locations along certain radial direction θ_r = 20º with the magnitudes of ε_r and ε_h decreasing from 2.3% to 2.2% and from 2.3% to 1.9% respectively. Meanwhile, 5 coordinates in Figure S6c represent the five individual radial directions θ (30º to 150º) where the ε_r of the biaxial strain was applied relative to the armchair orientation δ of the lattice parallel to the horizontal direction, x-axis. This follows that diverse biaxial strain conditions, such as ratios and applied directions, can be readily accessed in dome structure[3].

Note 2: Raman characterization of strain field over the dome

Raman measurement is one of the most common methods to determine and evaluate the existence and amount of strain in 2D materials, as the Raman peaks shift linearly with the strain applied[3, 4, 7, 8]. In this work, the location-dependent Raman measurements were conducted on the surface of the MoS_2 dome from the edge to center, and a quantitative analysis of the peak position of the Raman phonon modes enable to reaffirm the strain conditions provided by the analytical solution in Note 1.

As indicated in Fig S7, in the spectra extracted on the dome, both the peaks related to the strained monolayer of the dome and the peaks originated from the underlying bulk substrate can be observed. When the test sites were moving from the edge (bottom) to the center (top), the E_{2g}^1 and A_{1g} modes of bulk substrate remained at 383.3 and 408.3 cm^{-1}respectively, but the Raman peaks from the dome surface exhibited a clear soften mode (red shift). This clearly indicates the largest strain amount can be found at the summit of the dome and decline with location closed to the edge. Specifically, the out of plane A_{1g} mode featured a modest linear redshift with strain, while the in-plane E_{2g}^1 mode exhibited not only a larger redshift but also the double-degenerate with the increased strain, compared the freestanding monolayer MoS_2 flake. This could be explained as the transition between uniaxial strain to biaxial strain from the edge to the center of the dome. The proper amount of the anisotropic strains would break the in-plane symmetry of the monolayer MoS_2 flake, leading to the degeneracy breaks and the mode splits into two peaks as E_{2g}^{1-} and E_{2g}^{1+} respectively[7, 9]. Therefore, there is a clear peak splitting from the Raman spectra at the dome edge in Fig S7. This also validates the presence of the uni-axial strain provided by the analytical solution at the dome edge, where the amount of strain should be greater than the 1.5% of the reported value[9]. Moreover, as the biaxial strains avoid in-plane symmetry-breaking, there is no mode splitting and only linearly redshift with

greater strain[8]. With the dominance of the biaxial strains, in-plane symmetry-breaking becomes relieved and the mode splitting turns in to peak merging, with test sites away from the edge. Eventually, the isotropic biaxal is formed at the summit or the center of the dome, and the lattice remain in-plane symmetric and the in-plane mode acting as a sole E_{2g}^{1} peak at 372 cm^{-1}, which is also well matching the analytical result of the strain condition at the dome center.

The strain level at the dome summit can also be estimated by the peak shifts in E_{2g}^{1} peak, as only in-plane mode is more sensitive to the applied strain[8]. In this case, at the center of the dome the E_{2g}^{1} and A_{1g} modes are found to be shifted by 14.9±1.4 $cm^{-1}$and 6.3±1.4 cm^{-1} with respect to the values of the unstrained monolayer sample. Referring to $\varepsilon = (\omega - \omega_0)/\Delta_{E_{2g}^{1}}$ and the reported shift rate [2, 8], the total strain at the center of the dome can be estimated as 5.3±0.1%, having a good agreement with the analytical value, 4.6±0.1%. In addition, for the Grüneisen parameters governed by $\gamma_{E_{2g}^{1}} = (\omega - \omega_0)/(2\varepsilon\omega_0)$ [10], $\gamma_{E_{2g}^{1}} = 0.47$ and $\gamma_{A_g^1} = 0.17$ for two modes of this work agree well with those of previous works[2, 3, 5, 8, 11]. Therefore, we can conclude that the strain conditions resolved by the analytical solution are well consistent with the results provided by the Raman method, and it is valid for solving the complex strain field in the dome of this work.

Supplementary figures

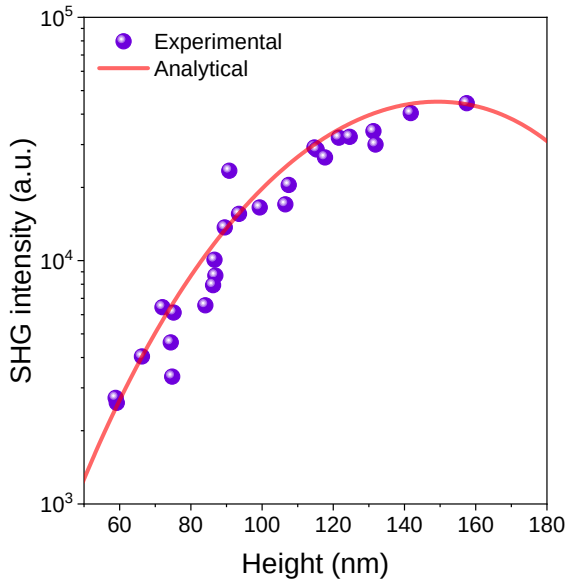

Figure S1 | SHG intensities collected at the top of WS_2 domes versus domes' height. Analytical values (red line) well matched with experimental results (purple spheres).

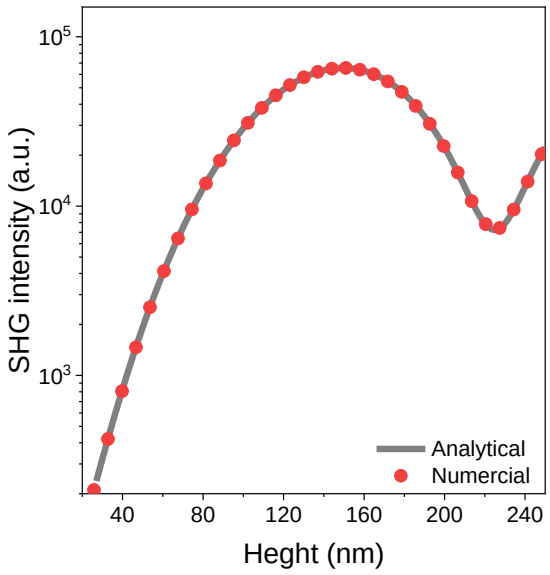

Figure S2 | Comparison of the SHG intensity as a function of the height of the MoS_2 domes using COMSOL simulation (red dots) and analytical method (grey line), where the excitation laser's wavelength was set at 900 nm.

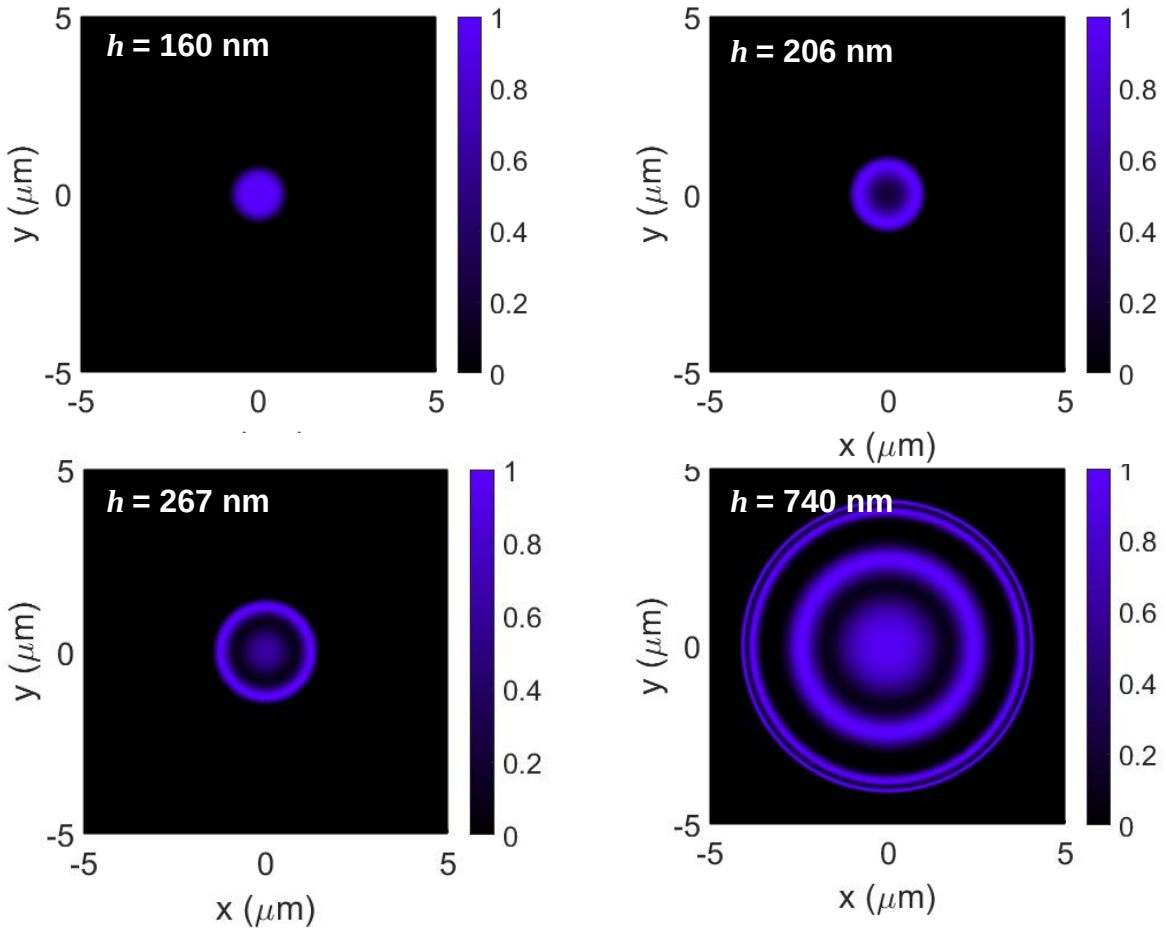

Figure S3 | Simulated intensity profiles (top view) of the normalized reflected SHG with height varying from 160 to 740 nm, according to the height profiles of the domes shown in the Figure 1d and the biggest dome shown in Figure 1d.

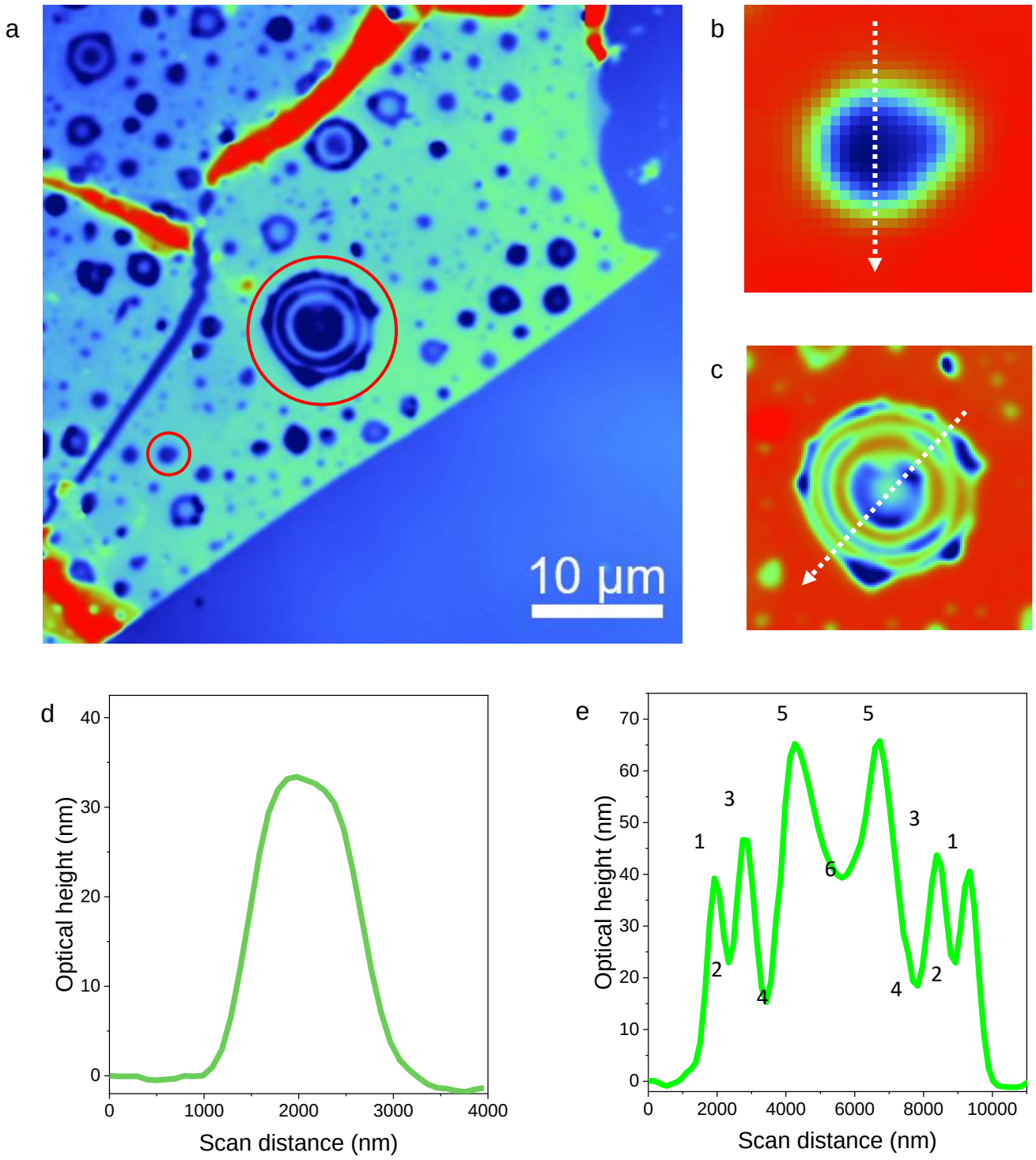

Figure S4 | Identification of the optical interference in the dome structure via Phase Shift Interferometry (PSI) with the wavelength of 535 nm. (a) PSI image of the dome samples within the same region shown in the Figure 1 a, b. **(b-c)** Zoom in PSI images of two different sized domes highlighted in the Figure S4a. **(d-e)** Optical height profiles extracted along the white dash lines over the domes shown in Figure S4b,c, where the optical height of the small

indicate the process on approaching the maximum path length difference before the phase shifts, while the optical height profile of the giant domes exhibit fringes induced by the optical interference with the separation height changes in the physical profile[12]. In Figure S4e, the optical intensity and distance between fringes would increase with the separation height. This could be explained by the light diffraction generated by the curvature of the hemisphere geometry when light transmits into the dome.

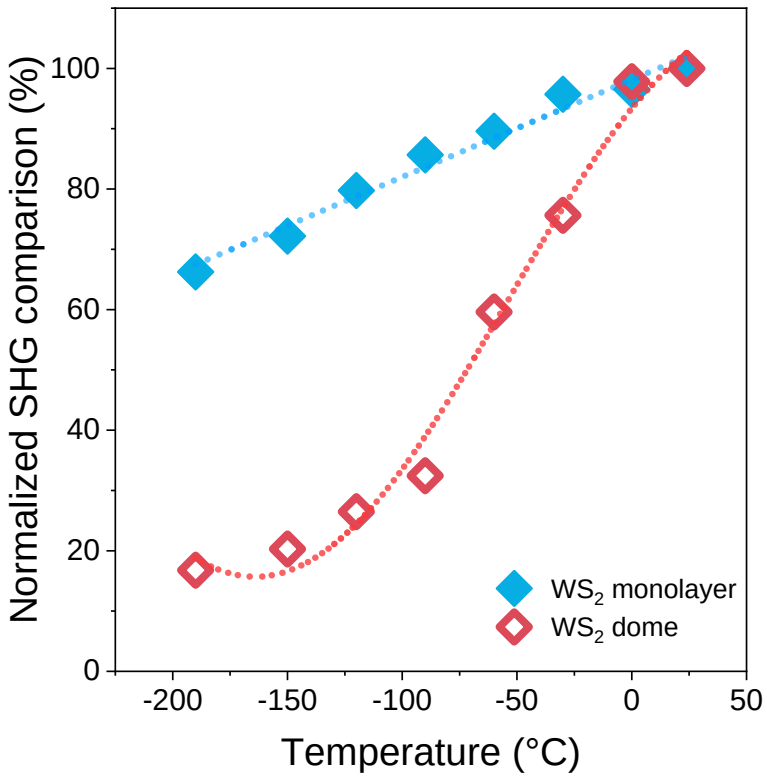

Figure S5 | Comaparsion of normalized SHG efficiency between the monolayer WS_2 dome (red open diamond) and the monolayer flake (blue solid diamond), with the temperature dropping from RT to -190 ºC.

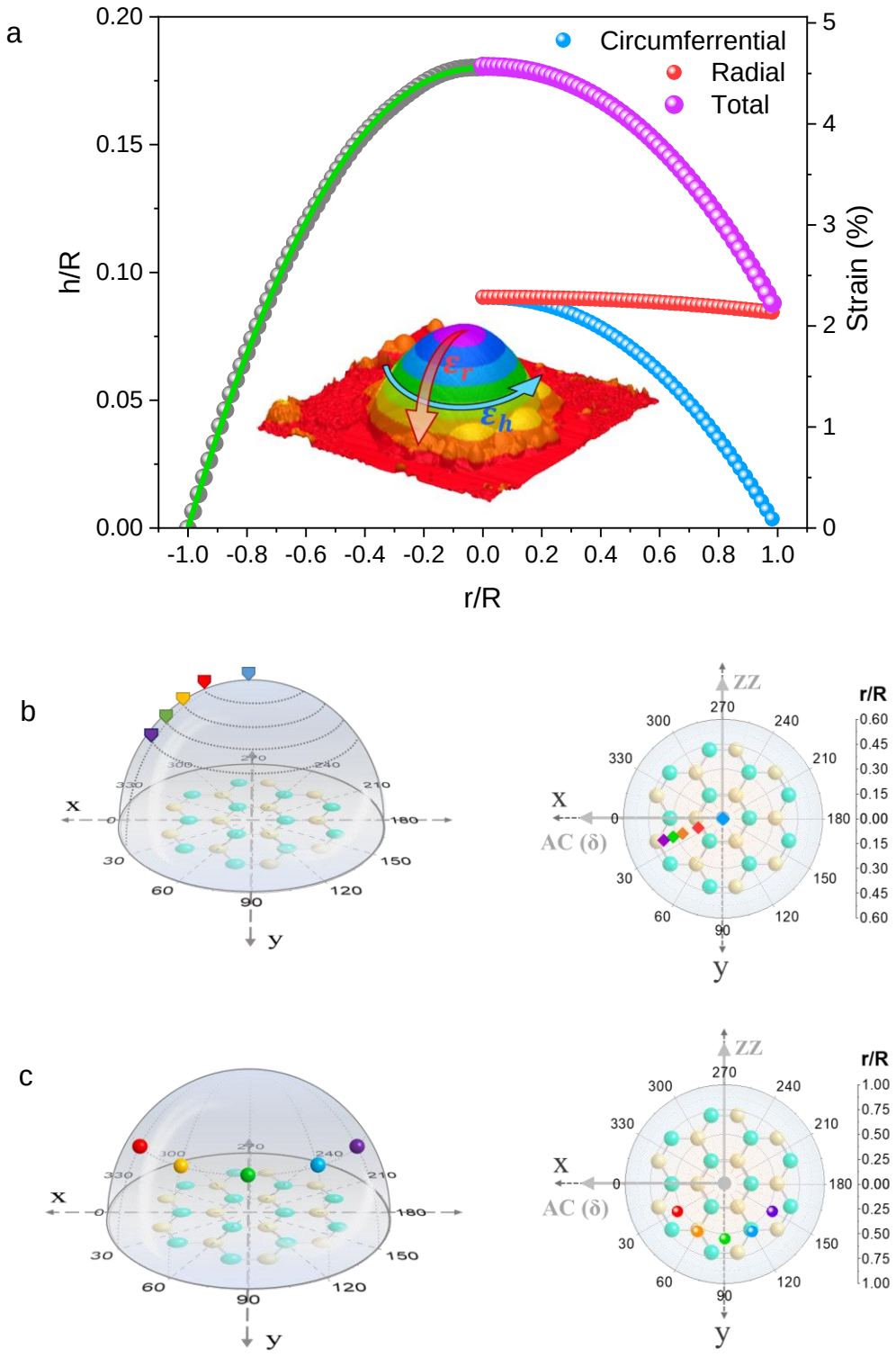

Figure S6 | Resolving strain effect induced by the dome structure. (a) Analytical results of the dome profile and the related strain components. Left axis: the normalized measured (grey) and analytical (green curve) dome profile with h/R ratio is 0.18; right axis: Normalized

components of strain distribution in radial (ε_r, red spheres¬) and circumferential (ε_h, blue spheres) directions resolved by analytical solution in terms of dome radius. Components ε_r and ε_h are represented as color-coded arrows on a 3D AFM image of the dome shown in the inset. (b-c) Locations on the dome surface that were given coordinates (r/R, θ_r, θ_h) for the various strain conditions, where r/R, θ_r and θ_h represent the radial distance away from the center, and principal orientations of the radial and circumferential strains applied respectively; Locations for the strain conditions in a specific direction away from the dome's center (r/R, 20º, 110º) with the r/R ranging from 0-0.39 labelled on the 3D dome schematic in (b), whose top view is depicted in the right panel; Locations in the circumferential direction at a fixed distance from the center of the dome (0.5, θ_r, θ_h), with the θ_r ranging from 30º to 150º coded in color as presented in 3D and project plot of a dome in (c). The lattice orientation of the dome as depicted in the schematics, where the Armchair direction (AC) is parallel to the horizontal axis (δ = 0º).

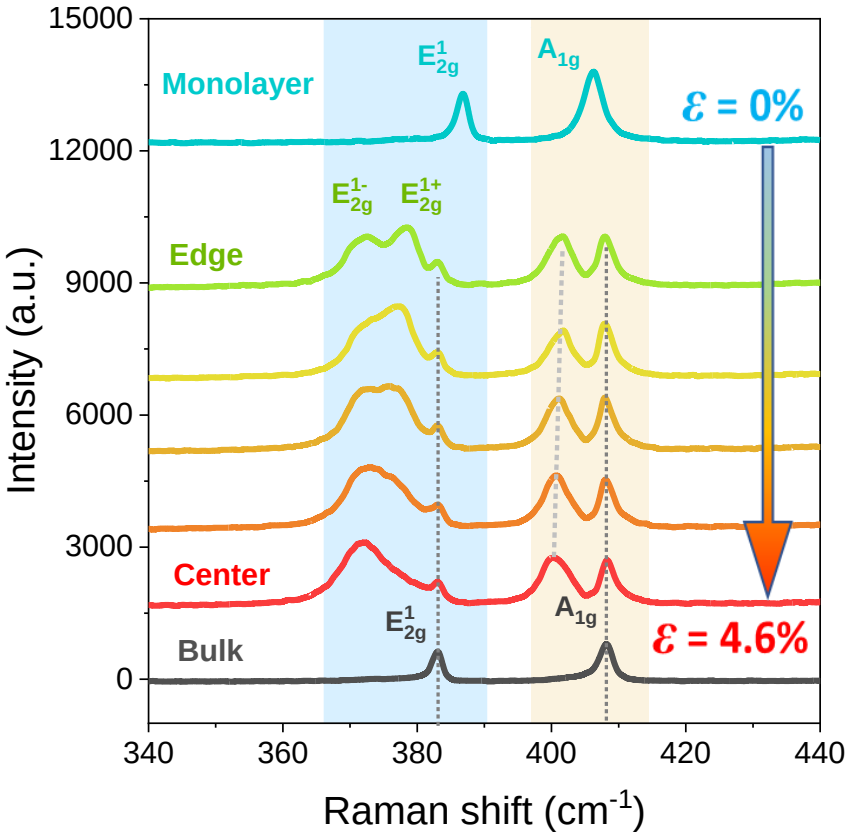

Figure S7 | Comparsion of Raman spectra obtained from monolayer MoS_2 flake and the monolayer MoS_2 dome. The E^1_{2g} (blue region) and A_{1g} (yellow region) phono modes exhibit obvious soften mode (red shift) compared with the spectrum of monolayer sample with 0% strain. The largest shifts in two mode peaks can be found at the center and the decline in the shifts occurred with radial distance from the center, where the split in Raman peak of E^1_{2g} is clearly observed at the edge of the dome, where the strain is closed to the uniaxial character. The splitting tends to disappear as the probing laser moves toward the center of the dome[4]. The varying difference in Raman shifts suggests that the dome center withstands the largest strain and the exponential decay trend in the strain distribution over the dome[2, 5], which has good consistency with the result generated by the analytical solution. The additional minor peaks at 382 and 409 cm^{-1} as highlighted by dark grey dash line are considered as the Raman signal from bulk MoS_2 beneath the dome membrane. (More details see SI note 2)

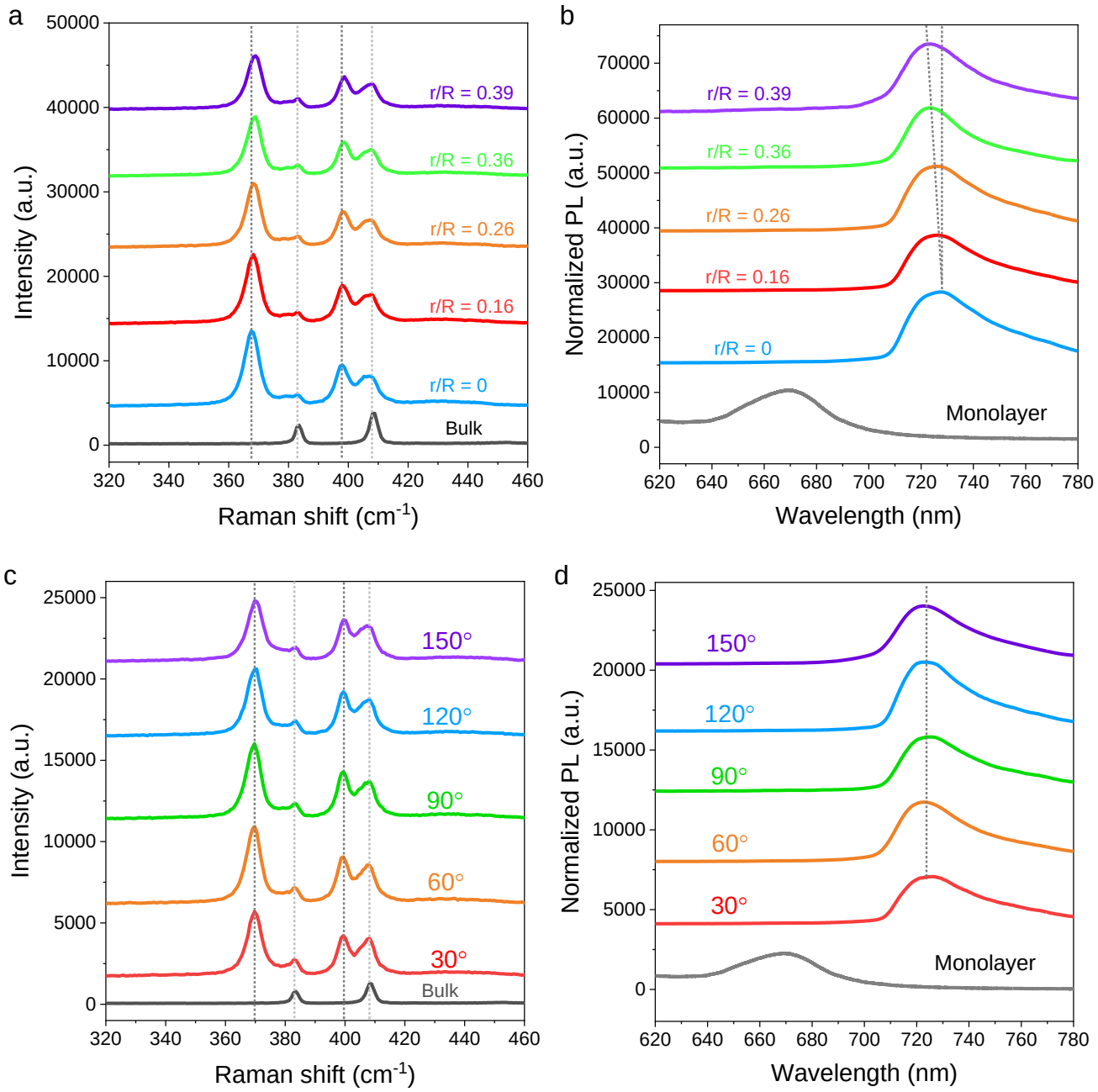

Figure S8 | Raman and Photoluminescence (PL) spectra extracted at the corresponding locations where various anisotropic SHG measurements were conducted. (a, b) Raman (a) and PL (b) spectra collected at locations varying from r/R = 0 to 0.39 in a certain orientation. The blue shifts in both plots suggest that the decreasing total strain at the site away from the dome summit, consistent with the reported influence of bi-axial strain on bandgap modulation[8], while there are minor shifts in the Raman and PL spectra from the sites with r/R = 0 and 0.16 due to the comparable total strain (0.02% of strain drop) between two sites. **(c, d)** Raman (c) and PL (d) spectra collected at locations with the same distance away from the dome summit but different strain orientation from 30º to 120º. Essentially identical PL and Raman spectra can be

extracted at all corresponding locations, suggesting that the strain conditions at those locations share the same magnitude regardless of strain orientations. The minor discrepancy of Raman and PL spectra among these test sites could be attributed to the artificial inaccuracy in the location selection.

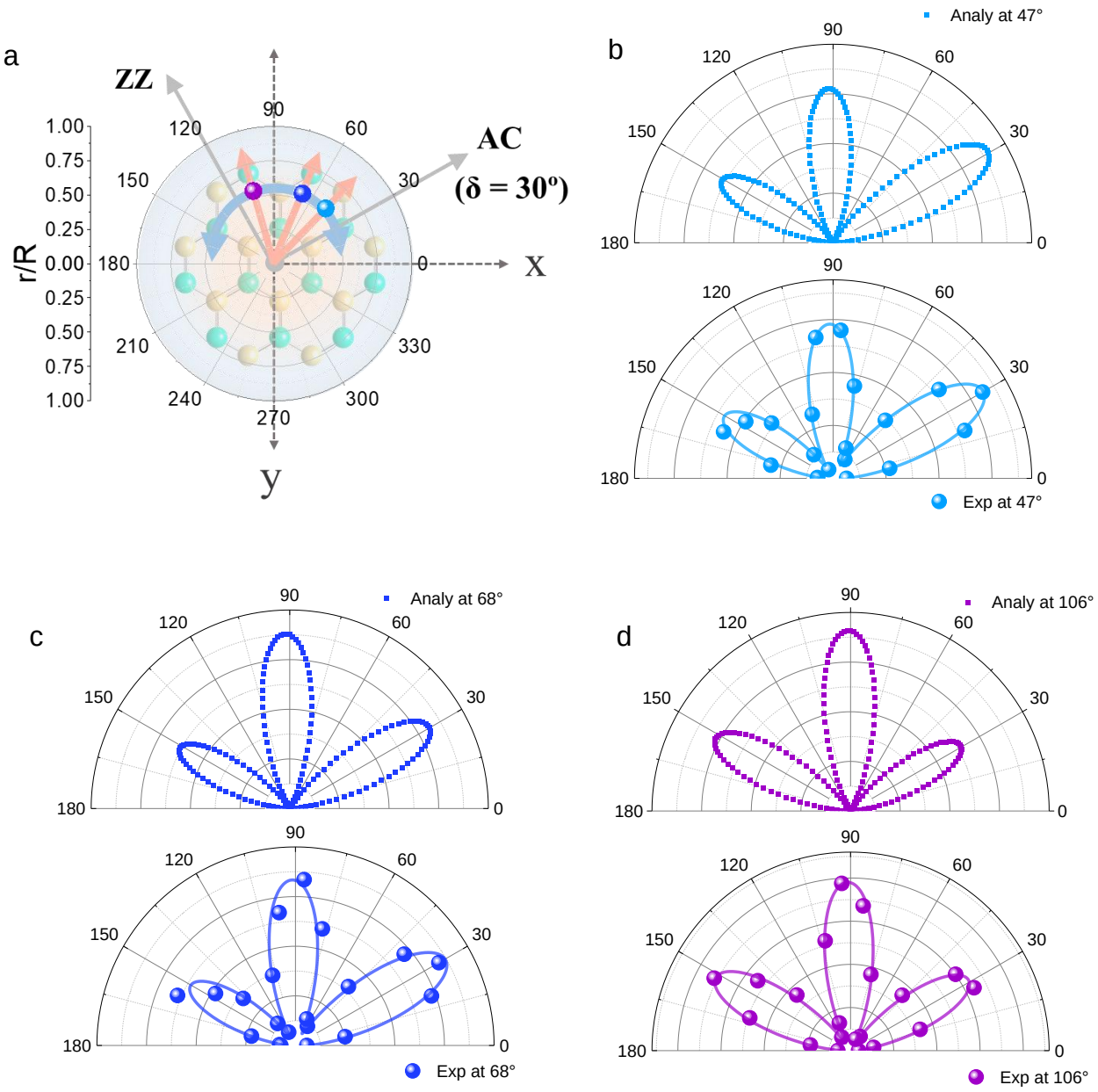

Figure S9 | Polarization-resolved SHG measurements to probe the lattice distortion induced by biaxial strain in various directions. (a) Schematics of the polarization-resolved SHG extracted at various locations along a hoop of the dome from the top perspective with orientation (δ) along the Armchair (AC) is 30º respect to horizontal axis. Radial and circumferential strains applied are represented by red and blue arrows respectively. **(b-d)** Top: Analytical polarization-resolved SHG at the locations shown in (a) with the different radial strain orientations (47°, 68° and 106°) but the same level; Bottom: Experimental results of

polarization-resolved SHG employed with the corresponding strain orientations and levels in relation to the sites on the dome structure as shown in (a).

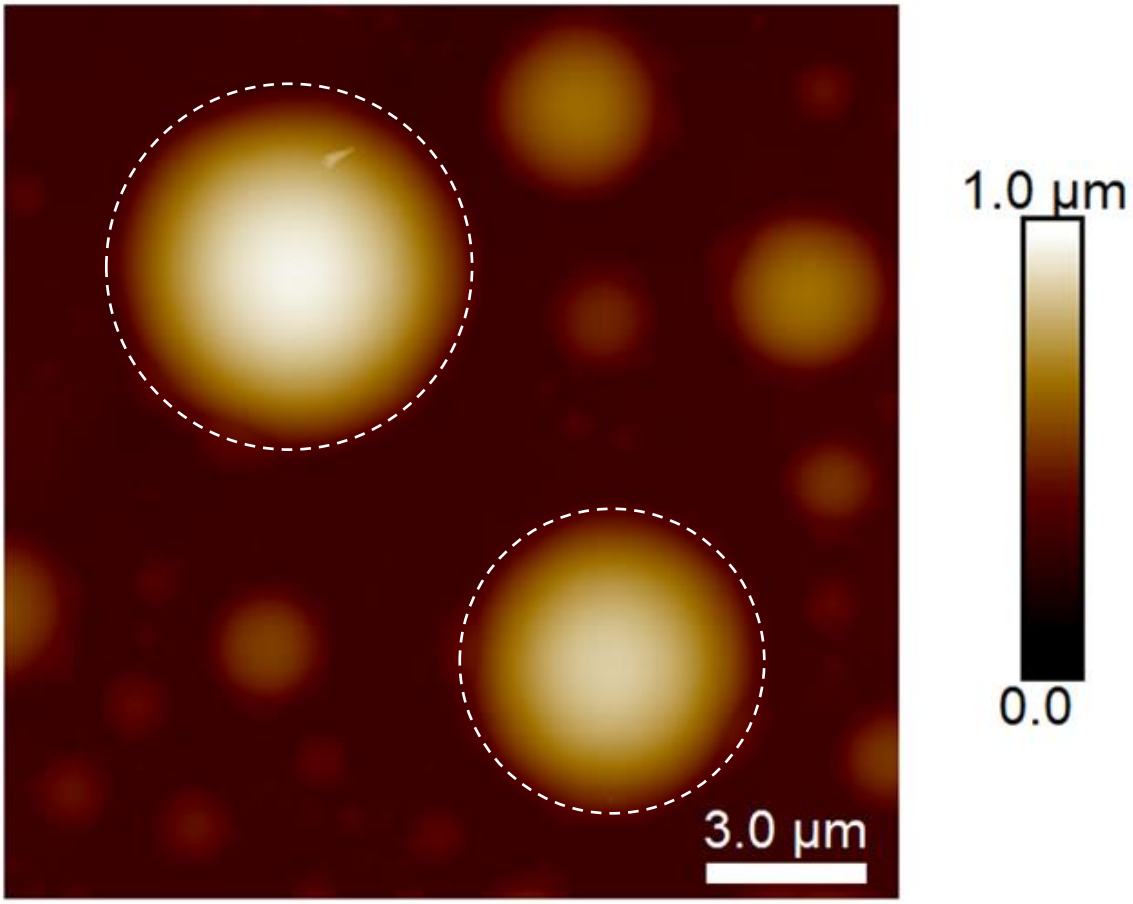

Figure S10 | Comparison between the footprint shape of domes and the round circle. Since the smaller domes normally have higher pressure gas, the side domes around the main big dome would intrude the main dome and influence the shape, which can further lead to the discrepancy of strain distribution compared to the analytical results.

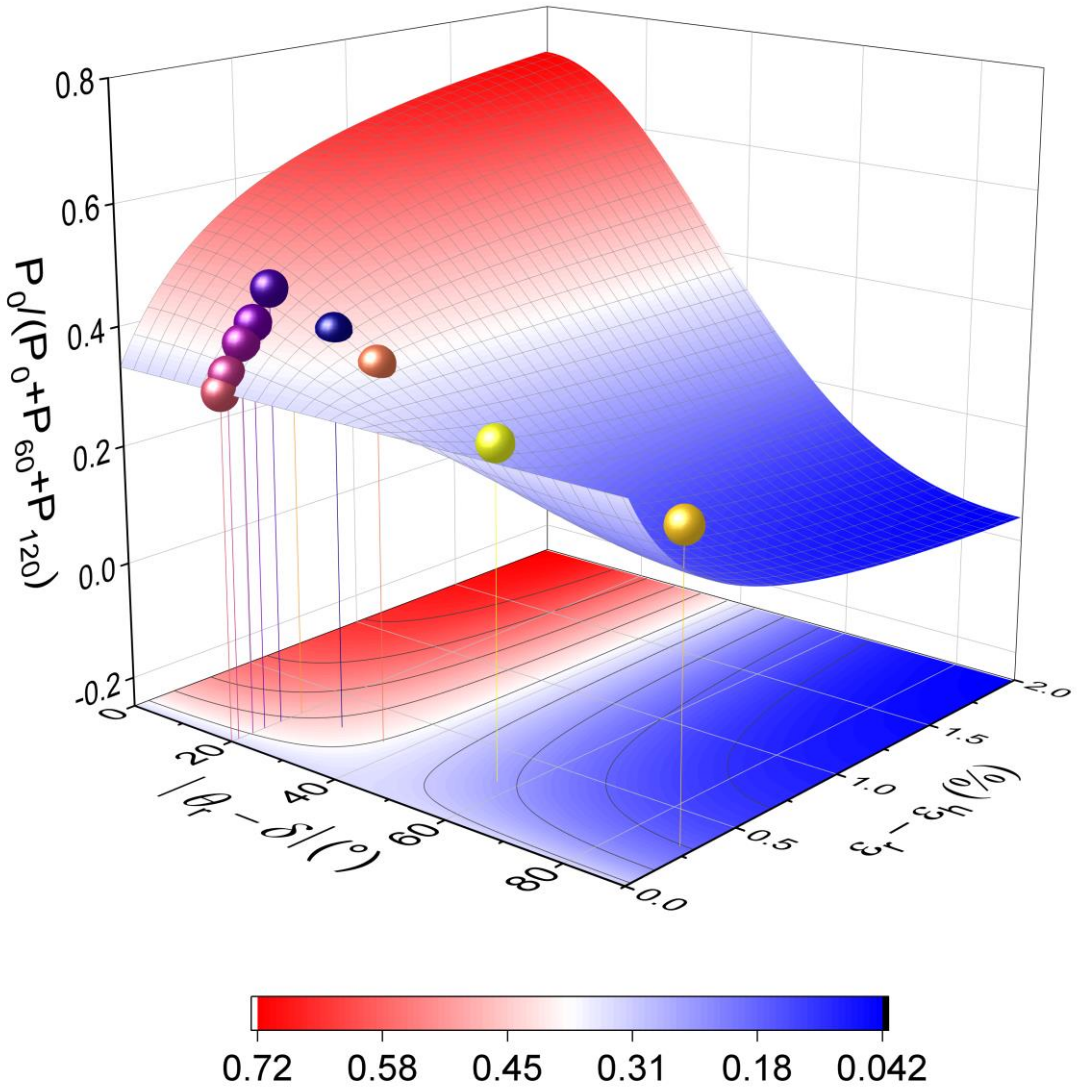

Figure S11 | Contour map showing the evolution of SHG polar pattern regarding strain difference ($\varepsilon_r - \varepsilon_h$) and principal strain orientation ($\theta_r - \delta$). $P_0 / (P_0+P_{60}+P_{120})$ represents the variation in the sizes of petals laying in 0º, 60º, 120º. The vales extracted from experimental SHG polar patterns are indicated by the color spheres, and contour map is coded by the analytical patterns, both of which have great consistency under various strain conditions.

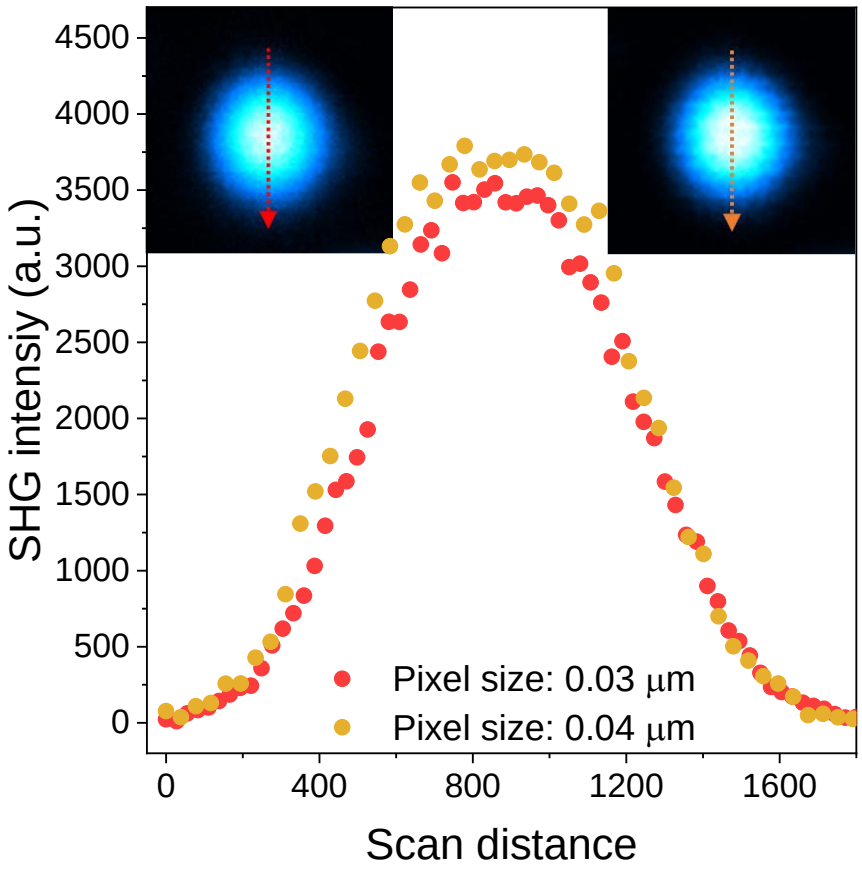

Figure S12 | Comparison of SHG intensity profiles extracted with different imaging resolutions. The intensity profiles suggest different capture resolution can provide comparable results, where the intensity discrepancy induced by the resolution difference is less than 7%. The 0.03 μm pixel size from the higher resolution imaging (red dots) enables the acquisition of more detailed information about intensity variation regarding locations, compared to the results governed by the larger pixel size (yellow dots). The insets are the mapping image of the same dome sample obtained under the same test condition but with different imaging resolution (Left: pixel size = 0.03 μm, Right: pixel size = 0.04 μm).

Reference list

1. Z. Dai, Y. Hou, D. A. Sanchez, G. Wang, C. J. Brennan, Z. Zhang, L. Liu and N. Lu, Phys Rev Lett **121** (26), 266101 (2018).
2. E. Blundo, T. Yildirim, G. Pettinari and A. Polimeni, Physical Review Letters **127** (4), 046101 (2021).
3. E. Blundo, E. Cappelluti, M. Felici, G. Pettinari and A. Polimeni, Applied Physics Reviews **8** (2) (2021).
4. C. Rice, R. J. Young, R. Zan, U. Bangert, D. Wolverson, T. Georgiou, R. Jalil and K. S. Novoselov, Physical Review B **87** (8), 081307 (2013).
5. E. Blundo, C. Di Giorgio, G. Pettinari, T. Yildirim, M. Felici, Y. Lu, F. Bobba and A. Polimeni, **7** (17), 2000621 (2020).
6. K. Elibol, B. C. Bayer, S. Hummel, J. Kotakoski, G. Argentero and J. C. Meyer, Scientific Reports **6**, 28485 (2016).
7. C. R. Zhu, G. Wang, B. L. Liu, X. Marie, X. F. Qiao, X. Zhang, X. X. Wu, H. Fan, P. H. Tan, T. Amand and B. Urbaszek, Physical Review B **88** (12) (2013).
8. D. Lloyd, X. Liu, J. W. Christopher, L. Cantley, A. Wadehra, B. L. Kim, B. B. Goldberg, A. K. Swan and J. S. Bunch, Nano Letters **16** (9), 5836-5841 (2016).
9. Z. Li, Y. Lv, L. Ren, J. Li, L. Kong, Y. Zeng, Q. Tao, R. Wu, H. Ma, B. Zhao, D. Wang, W. Dang, K. Chen, L. Liao, X. Duan, X. Duan and Y. Liu, Nature Communications **11** (1), 1151 (2020).
10. J. Zabel, R. R. Nair, A. Ott, T. Georgiou, A. K. Geim, K. S. Novoselov and C. Casiraghi, Nano Letters **12** (2), 617-621 (2012).
11. D. Tedeschi, E. Blundo, M. Felici, G. Pettinari, B. Liu, T. Yildrim, E. Petroni, C. Zhang, Y. Zhu and S. Sennato, Advanced Materials **31** (44), 1903795 (2019).
12. J. Yang, Z. Wang, F. Wang, R. Xu, J. Tao, S. Zhang, Q. Qin, B. Luther-Davies, C. Jagadish, Z. Yu and Y. Lu, Light: Science & Applications **5** (3), e16046-e16046 (2016).